MATERIALS SCIENCE

Highly mobile hot holes in $Cs_2AgBiBr_6$ double perovskite

Heng Zhang[1], Elke Debroye[2]*, Wenhao Zheng[1], Shuai Fu[1], Lucia D. Virgilio[1], Pushpendra Kumar[1], Mischa Bonn[1], Hai I. Wang[1]*

Highly mobile hot charge carriers are a prerequisite for efficient hot carrier optoelectronics requiring long-range hot carrier transport. However, hot carriers are typically much less mobile than cold ones because of carrier-phonon scattering. Here, we report enhanced hot carrier mobility in $Cs_2AgBiBr_6$ double perovskite. Following photoexcitation, hot carriers generated with excess energy exhibit boosted mobility, reaching an up to fourfold enhancement compared to cold carriers and a long-range hot carrier transport length beyond 200 nm. By optical pump–infrared push-terahertz probe spectroscopy and frequency-resolved photoconductivity measurements, we provide evidence that the conductivity enhancement originates primarily from hot holes with reduced momentum scattering. We rationalize our observation by considering (quasi-)ballistic transport of thermalized hot holes with energies above an energetic threshold in $Cs_2AgBiBr_6$. Our findings render $Cs_2AgBiBr_6$ as a fascinating platform for studying the fundamentals of hot carrier transport and its exploitation toward hot carrier–based optoelectronic devices.

INTRODUCTION

Optical excitation of semiconductors by photons with energy ($h\nu$) exceeding their bandgap (E_g) creates energetic, "hot" carriers with an excess energy $E_{ex} = h\nu - E_g$. These initially nonthermalized hot carriers can reach thermalization with a defined electronic temperature following the Fermi-Dirac distribution via carrier-carrier interactions in tens to hundreds of femtoseconds (fs) (*1*–*3*). The thermalized hot carriers can subsequently dissipate their excess energy to the lattice, becoming "cold" carriers at the band edge within a few picoseconds (ps) in most conventional semiconductors (*4*, *5*). The ultrafast energy loss during hot carrier cooling represents one of the major loss channels for solar cells, limiting the energy conversion efficiency to ~33.7% (so-called Shockley-Queisser limit) (*6*, *7*). Harvesting hot carriers before their relaxation is a much sought-after goal for achieving efficient optoelectronics, specifically photovoltaics (*8*, *9*). One of the main challenges is the relatively short transport length of hot carriers before dissipating their excess energy to the environment. This is due to the typically short hot carrier lifetimes combined with substantially reduced mobilities of hot charge carriers resulting from the enhanced momentum scattering rates, as reported in conventional semiconductors (e.g., Si and GaAs) (*4*, *10*, *11*).

Recent reports on remarkably long-lived hot carriers (with lifetimes over 100 ps) in lead halide perovskites have attracted enormous interest in exploiting hot carriers for fundamental research and developing efficient hot carrier–based optoelectronic devices (*5*, *12*). In addition to the lifetime, some recent ultrafast spectroscopic studies on perovskites have reported fascinating hot carrier transport properties on (sub-)picosecond time scales following light absorption and charge generation. For instance, Sung *et al.* (*13*) have reported that hot carriers can propagate more than 150 nm within 20 fs upon photon absorption in a methylammonium lead iodide system applying transient absorption (TA) microscopy, providing experimental evidence for ballistic transport (i.e., charge transport without scattering) of hot carriers on a sub–20 fs time scale. For the transport of relatively long-lived hot carriers from subpicoseconds to tens of picoseconds, different and even contradictory spectroscopic results have been reported. For instance, using the same techniques as by Sung *et al.* (*13*) with, however, a lower time resolution (more than 300 fs), Guo and colleagues (*14*) observed a quasi-ballistic transport in $MAPbI_3$ over 200 nm in the first 300 fs, followed by a diffusive transport regime of nonequilibrium hot carriers persisting for tens of picoseconds over a distance of 600 nm. This ultrafast, long-range transport seems to imply higher mobility for hot carriers than for cold ones. On the other hand, combining TA and terahertz spectroscopy, Monti *et al.* (*15*) reported that, while hot carriers show a long lifetime over 100 ps in a mixed Pb-Sn halide perovskite as observed by TA, time-resolved terahertz spectroscopy shows no difference in photoconductivity between hot and cold carriers. This led to the conclusion that hot carriers display mobilities similar to cold carriers. Clearly, hot carrier transport properties in metal halide perovskites, especially the transient hot carrier mobility, have so far remained elusive and merit further investigation.

Among the metal halide perovskites, $Cs_2AgBiBr_6$ double perovskite has emerged as a promising alternative to toxic, unstable lead halide perovskites for various optoelectronic applications owing to its outstanding chemical stability, nontoxicity, and outstanding optoelectronic properties, e.g., long carrier lifetimes (*16*, *17*) and large carrier diffusion lengths (*18*, *19*). In particular, $Cs_2AgBiBr_6$ double perovskite has shown exceptional performance for high-energy photon detection applications: For instance, it exhibits excellent x-ray detection with a low detection limit (*17*, *20*, *21*). Therefore, a study of hot carrier transport in $Cs_2AgBiBr_6$ double perovskites following high-energy photoexcitations is of great fundamental interest and could provide insights into their further optoelectronic applications. Here, using optical pump–terahertz probe (OPTP)

[1]Max Planck Institute for Polymer Research, Ackermannweg 10, 55128 Mainz, Germany. [2]Department of Chemistry, KU Leuven, Celestijnenlaan 200F, 3001 Leuven, Belgium.
*Corresponding author. Email: elke.debroye@kuleuven.be (E.D.); wanghai@mpip-mainz.mpg.de (H.I.W.)

spectroscopy, we observe anomalously high transient mobility of hot carriers within the first ~3 ps after photoinjecting hot carriers in $Cs_2AgBiBr_6$ double perovskites. This contrasts with conventional semiconductors, where hot carriers have lower mobilities than those of band-edge states due to enhanced electron-phonon scattering. By optical pump–infrared (IR) push-terahertz probe (PPP) spectroscopy, we provide experimental evidence that highly mobile hot holes, rather than hot electrons, are primarily responsible for the observed high transient mobility in $Cs_2AgBiBr_6$ double perovskites. Furthermore, frequency-resolved photoconductivity measurements reveal that the high mobility of charge carriers in the hot states originates from reduced momentum scattering events, i.e., longer scattering time. We rationalize our observation by including (quasi-)ballistic transport of the thermalized hot holes with sufficient kinetic energy in $Cs_2AgBiBr_6$. Our results render $Cs_2AgBiBr_6$ double perovskites as an interesting platform for hot carrier studies for both fundamental physics and device applications, exploiting their high mobility.

RESULTS

A schematic illustration of the $Cs_2AgBiBr_6$ double perovskite crystal structure is shown in Fig. 1A. At room temperature, $Cs_2AgBiBr_6$ has a cubic phase, in which the monovalent Ag^+ and trivalent Bi^{3+} cations are centered alternately in each of the octahedra that consist of six monovalent Br^- anions (*22*). The Cs^+ cations are situated in the corner-shared cuboctahedral cavities. Figure 1B illustrates the x-ray diffraction (XRD) pattern of the prepared $Cs_2AgBiBr_6$ double perovskite thin film (synthesis details in the Supplementary Materials). All peaks are in good agreement with theoretical calculations and previous experimental results for $Cs_2AgBiBr_6$, ruling out the presence of other phases and unreacted precursors in the synthesized sample (*23*, *24*).

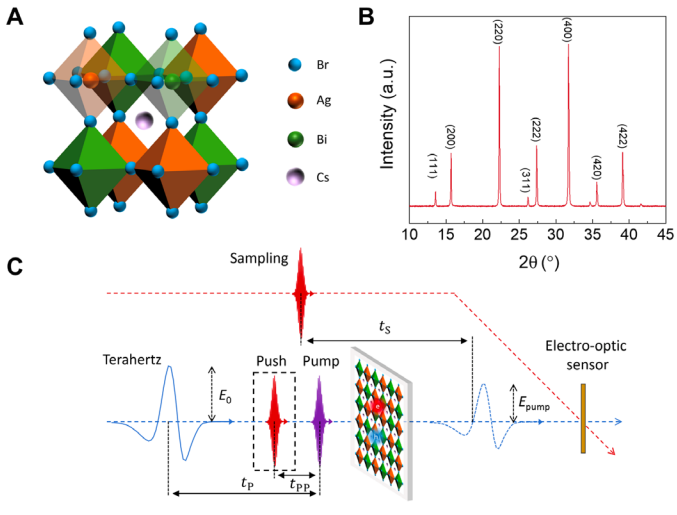

Fig. 1. Sample characterization and terahertz spectroscopy setup. (**A**) Atomic structure and (**B**) XRD pattern of the $Cs_2AgBiBr_6$ double perovskite. a.u., arbitrary unit. (**C**) Experimental layout for OPTP or PPP spectroscopy. The push pulse (marked in red in the dashed box) can be selectively switched on and off depending on the measurement mode. For the OPTP studies (by blocking the push pulse), the setup measures the pump-induced (the purple pulse) terahertz field absorption to quantify the photoconductivity dynamics of the excited charge carriers by controlling the pump-probe delay t_P. The electric field of the transmitted terahertz pulse through the sample (the blue dashed pulse) is measured via free-space electro-optic sampling in a ZnTe crystal (the orange rectangle) by a third short pulse (~800 nm, with a duration of ~100 fs; the top red pulse), controlling the delay between the sampling and the transmitted terahertz pulse t_S. For the PPP studies, the push pulse (bottom red) is switched on at a controlled pump-push delay time t_{PP} to reexcite the system.

To investigate the dynamics and transport properties of hot carriers following optical excitation, we use ultrafast, contact-free terahertz spectroscopy, as illustrated in Fig. 1C, to directly monitor the photoconductivity of the charge carriers with a ~200 fs time resolution. The setup can be operated in two measurement modes: the normal mode for OPTP spectroscopy and a customized mode for PPP spectroscopy by introducing a second excitation beam (i.e., push) at a tunable pump-push delay t_{PP}. In a typical OPTP measurement, an optical pulse with ~100 fs duration and tunable photon energies above the semiconductor bandgap generates free charge carriers in the sample by exciting electrons from the valence to the conduction band. After a pump-probe delay time t_P, a terahertz pulse propagating collinearly through the sample probes the transient photoconductivity σ ($=n \cdot e \cdot \mu$, with n as the photogenerated carrier density, μ as the charge mobility, and e as the elementary charge), which is linearly proportional to the pump-induced, relative attenuation of the terahertz electric field ($-\Delta E/E_0$, with $\Delta E = E_{pump} - E_0$, here, E_0 and E_{pump} are the transmitted terahertz pulse without and with pump, respectively). The transmitted terahertz electric field in the time domain is measured by a third sampling pulse (~100-fs duration, with the central energy of ~1.55 eV) via free-space electro-optic sampling in a ZnTe crystal (*25*, *26*). Note that, here, for OPTP measurements, we probe the photoconductivity by recording the pump-induced modulation in the terahertz peak field (via fixing the sampling beam to the peak of terahertz pulses). The time resolution (~200 fs) for OPTP measurements is therefore limited by the duration of the pump and sampling pulses rather than by the duration of terahertz pulses (in a picosecond time scale). For the PPP experiment, a push pulse in the near-IR range (here, 1.55 eV) reexcites the charge carriers from the cold states at the band edge to hot states at a controlled pump-push delay time t_{PP}.

Observing highly conductive hot carriers by OPTP measurements

In Fig. 2A, we show the ultraviolet-visible (UV-vis) absorption spectrum of a $Cs_2AgBiBr_6$ crystalline thin film used for terahertz spectroscopy studies, with a thickness of approximately 200 nm characterized by atomic force microscopy (see fig. S1). $Cs_2AgBiBr_6$ is an indirect semiconductor with a band-edge absorption involving an *X*-*L* transition in the momentum space (*27*, *28*). Using a Tauc plot, we infer an indirect bandgap of ~2.17 eV (see fig. S2), falling into the range of previously reported values (from 1.83 to 2.25 eV) (*29*, *30*). The terahertz transmission through unpumped sample is shown in fig. S3. The selected pump wavelengths for OPTP measurements are denoted with dashed lines in the absorption spectrum in Fig. 2A, spanning from the near band edge (with $h\nu$ ~ 2.43 eV) to the high energetic states in the conduction/valence band (with $h\nu$ up to ~3.65 eV). To avoid higher-order recombination processes (e.g., Auger recombination), we excite the sample with relatively low fluence (~10^{13} photons cm^{-2}). Within the applied range of fluences, the photoconductivity shows a linear dependence on the fluence, as shown in fig. S4.

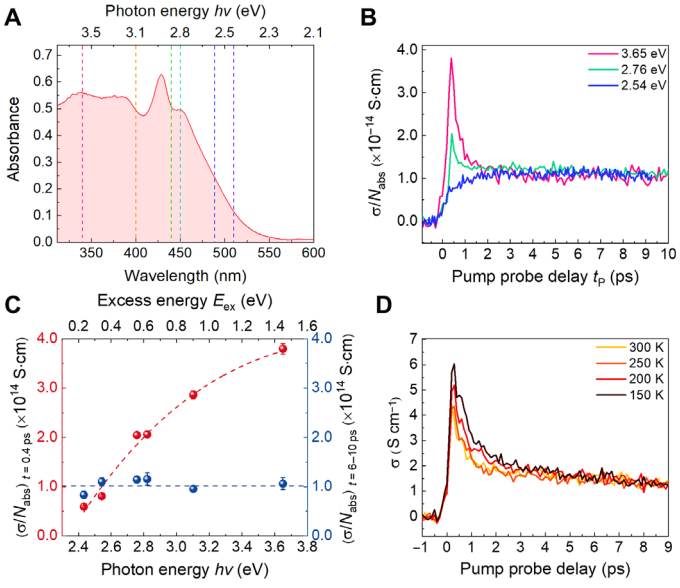

Fig. 2. Photon energy– and temperature-dependent photoconductivity dynamics. (**A**) Absorption spectrum of $Cs_2AgBiBr_6$. The vertical dashed lines indicate the pump wavelengths used in the OPTP measurements. (**B**) Pump photon energy ($h\nu$)–dependent photoconductivity σ, divided by the absorbed photon density, N_{abs}, as a function of pump-probe delay time t_P for three exemplary excitation energies. (**C**) The photoconductivity at $t_P = 0.4$ ps [at which the photoconductivity reaches a maximum for above −2.76-eV excitations in (B)] (left axis and red data points) and the average value from 6 to 10 ps for each photon energy (right axis and blue data points), as a function of the pump photon energy (bottom axis) and excess energy (top axis). The dashed lines are guides to the eyes. The error bar represents the uncertainty in the fluence measurements for quantifying the absorbed photon density and the measurement noise level. (**D**) Temperature-dependent photoconductivity dynamics, following excitation at 3.1 eV with a fluence of 2.91×10^{14} cm^{-2}.

To unveil the role of the excess energy on hot carrier dynamics, we compare the photoconductivity of $Cs_2AgBiBr_6$ divided by the absorbed photon density, N_{abs}, following optical excitations with different photon energies. Here, the real part of the photoconductivity is measured by monitoring the pump-induced absorption at the peak of the terahertz field (*31*, *32*). In principle, the time-resolved photoconductivity $\sigma(t_P)$ is determined by the product of the carrier density $n(t_P)$ [with $n(t_P = 0) \propto N_{abs}$] and charge mobility $\mu(t_P)$ in the sample: $\sigma(t_P) = e \cdot n(t_P) \cdot \mu(t_P)$. As shown in Fig. 2 (B and C), we reveal an intriguing difference between dynamics for excitations with photon energies above and below 2.76 eV (see all the photoexcitations in fig. S5). When the pump photon energy, $h\nu$, is below ~2.7 eV (e.g., for excitations at 2.43 and 2.54 eV), the photoconductivity shows a gradual increase during the first 2 to 3 ps, followed by a plateau for tens of picoseconds. We note that the rise in photoconductivity is much slower than the time resolution of the setup (~200 fs). Similar photoconductivity dynamics in lead halide perovskites following close to band edge excitations have previously been assigned to polaron formation, during which the charge scattering rate is reduced (*33*, *34*). In line with this assignment, recent studies have also reported polaron formation in $Cs_2AgBiBr_6$ double perovskites in the first few picoseconds (*23*, *24*). During polaron formation, the effective mass of charge carriers is expected to increase, lowering the charge mobility. Simultaneously, the momentum scattering time of the charge carrier can be, however, substantially increased because of the screening protection of the polaron states, balancing out the effect of the enhanced effective mass on the charge carrier mobility (*12*, *35*, *36*). The slow rise of the photoconductivity indicates that the formed polarons are more mobile than the nascent carriers near the band edge, primarily due to the substantially reduced scattering rate. On the other hand, for $h\nu > 2.7$ eV, the photoconductivity exhibits a swift rise within a few hundreds of femtoseconds, dropping in the following 2 to 3 ps to a constant conductivity. In Fig. 2C, we summarize the photoconductivity amplitude at ~0.4 ps (at which photoconductivities with $h\nu > 2.7$ eV show a peak) and the averaged plateau value from 6 to 10 ps, as a function of photon energy $h\nu$ and excess energy E_{ex}. Despite the distinctive dynamics in the first 3 ps, the photoconductivity ultimately reaches, within experimental uncertainty, the same value for all excitation wavelengths. The identical $\frac{\sigma}{N_{abs}}$ value [$\propto n(t_P) \cdot \mu(t_P)$] from 3 to 10 ps suggests that photoexcited charge carriers do not recombine in the first 3 ps via, e.g., charge trapping. Instead, the result indicates that (i) the photon-to-charge conversion efficiency, i.e., the quantum efficiency of charge generation, is independent of excitation wavelength; (ii) the charge carriers reach the same final polaron states of within ~ 3 ps following excitation; and (iii) above a photon energy threshold of ~2.7 eV, a short-lived enhanced photoconductivity is observed, increasing in amplitude with increasing photon energy. The intriguing charge carrier dynamics transition at ~2.7 eV is markedly different from previously reported photoconductivity dynamics for lead-based halide perovskites, in which the charge carrier dynamics are consistently characterized by a fast, subpicosecond to picosecond rise, followed by a long-lived photoconductivity plateau (similar to the dynamics following a 2.54-eV excitation as shown in Fig. 2B) (*33*, *34*).

After establishing that polarons are formed independent of the excitation pathways, we now turn to the initially enhanced photoconductivity decaying within 3 ps. As the charge population remains unchanged in this time window, our result suggests a higher mobility of hot carriers than that of the final polaron states. As plotted in Fig. 2C, the peak mobility of hot carriers increases with the pump excess energy, indicating a correlation between high energy states and the high mobility of hot carriers. For $h\nu = 3.65$ eV (excess energy of ~1.5 eV), the peak mobility of the hot carriers reaches an almost four times higher value than that of cold carriers. In conventional semiconductors, hot carriers experience enhanced momentum scattering and thus have a lower mobility (*4*, *10*, *11*). To further confirm the conductive nature of hot carriers in $Cs_2AgBiBr_6$ double perovskite, we conduct temperature-dependent photoconductivity measurements as shown in Fig. 2D. Here, we limit the measurement range from 150 to 300 K to avoid the phase transition of $Cs_2AgBiBr_6$ at 122 K (*22*). At low temperature, we observe a higher peak photoconductivity due to a slowdown of hot carrier thermalization and cooling (quantified in fig. S6). We can rule out the temperature-induced absorption changes as the primary origin for the observed enhanced photoconductivity at low temperature, as previous studies reported minor changes in the bandgap of double perovskites while lowering the temperature down to cryogenic temperatures. Furthermore, to provide a direct support for such a claim, we measure and analyze frequency-resolved photoconductivity at 5 ps following optical excitation, as shown in fig. S7. The charge carrier density is found to be nearly identical on the basis of Drude-Smith (DS) analysis for both 300 and 150 K (manifested by the identical

plasma frequency in table S1). From the long-time (~10 ps) signal, it is evident that the conductivity of equilibrated polarons is temperature independent over used temperature range, possibly due to impurity scattering.

Highly mobile hot holes revealed by the PPP spectroscopy

To unambiguously confirm the high mobility of hot carriers with photon energy above 2.76 eV and to further disentangle the conductivity contributions from hot electrons and holes, we conduct optical PPP experiments (*37*). In these experiments, we photogenerate charge carriers following 3.1-eV excitations. After the hot carrier cooling and relaxation into the polaron states (within 3 ps), we reexcite the cold carriers by an IR pulse with a photon energy below the bandgap of $Cs_2AgBiBr_6$ (2.17 eV). On the basis of the previously reported band structure, the conduction band (CB) has a gigantic band splitting (more than 1.8 eV at the *L* point, the conduction band minimum) due to a strong spin-orbit coupling in $Cs_2AgBiBr_6$, while no such splitting is observed in the valence band (VB). Furthermore, the density of electronic states in the valence band is much higher and more extended than that of the conduction band (*28*, *38*). Here, we select a 1.55-eV excitation as the push pulse to selectively reexcite only cold holes, as shown schematically in Fig. 3A. In Fig. 3B, following the push excitation at ~8.2 ps after the pump pulse, we observe a transient increase in photoconductivity. The conductivity enhancement by the push increases with the fluence of push pulses at a constant incident pump fluence of 1×10^{14} cm^{-2}, as illustrated in Fig. 3C. The lifetime of the increased photoconductivity is consistent with the hot carrier cooling time following the first excitation. We exclude the contribution of two-photon absorption to the photoconductivity in our study by blocking the first 3.1-eV pump: With only the push pulse as the excitation, we do not observe any photoconductivity signal (with a fluence of ~1.6×10^{15} cm^{-2}), as seen in Fig. 3C. As only cold holes can be reexcited by the push pulse, we conclude that hot holes have higher mobility than the corresponding cold ones. Combined with the band structure, this result can explain the observed photoconductivity transition at $h\nu > 2.7$ eV. The first direct band transition (at the *X* symmetry point) in double perovskites is around 2.8 eV (*27*, *39*, *40*). When exciting the sample with $h\nu$ = 2.43 and 2.54 eV, the excess energy of the photons will primarily end up in the hot electrons due to the relatively flat and narrow first conduction band. The observed slow rise of the photoconductivity implies that (with a relatively low excess energy of ~0.4 eV) hot charge carriers are less mobile than the cold ones. For $h\nu > 2.7$ eV, because of the continuous, high density of hole states in the valence band, excess energy in pump photons will predominantly go into hot holes. This leads to a transient enhancement of photoconductivity due to the highly mobile hot holes.

Significantly reduced scattering rate of hot carriers demonstrated by frequency-resolved photoconductivity spectra

To gain more insights into the highly mobile hot carriers in double perovskites, we further analyze the time evolution of hot carrier transport properties by recording photoconductivity spectra at various delay times (see experimental details in the Supplementary Materials). Since the photoconductivity change is faster than the terahertz pulse duration in our case, extra care needs to be taken for tracking the pump-induced terahertz changes in the time domain (*31*, *41*). Here, to conduct time-domain spectroscopy (TDS) in our rapidly decaying photoconductivity dynamics (in the first 2 to 3 ps), we record the time evolution of the probing terahertz pulse by moving the pump and sampling stages simultaneously at a given pump-probe delay. In this way, one can ensure that different parts of the terahertz pulse "see" the same transient photoconductivity. In the Supplementary Materials, we detail this measurement protocol and discuss its pros and cons over the TDS measurement protocol in which only the sampling pulse delay stage is moved. Figure 4A shows the early time evolution of the time-resolved terahertz electric field change $-\Delta E$ induced by a 3.1-eV photoexcitation with an absorbed photon density of ~1.02×10^{14} cm^{-2}. The buildup of the picosecond free-carrier conductivity is stabilized in phase at ~0.7 ps, while changing only in intensity afterward. As a representative example, Fig. 4B shows a series of real and imaginary components of the complex photoconductivity at different pump-probe delay times.

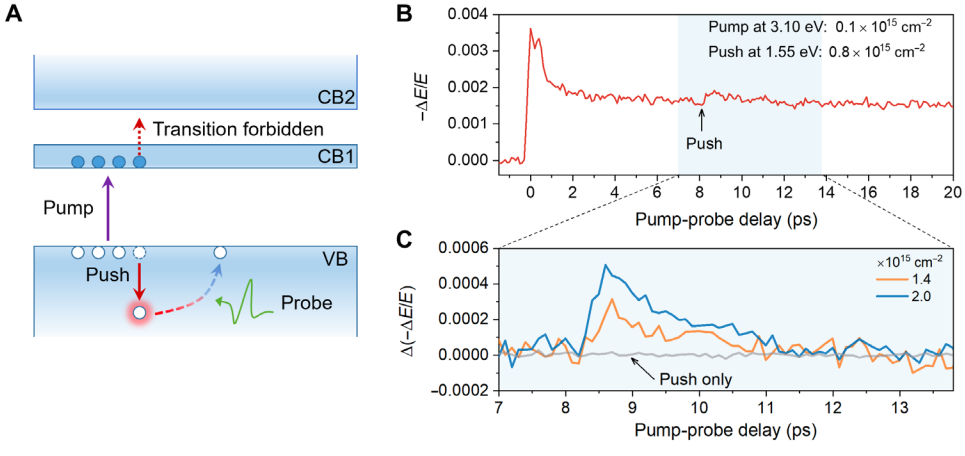

Fig. 3. PPP spectroscopy. (**A**) Schematic illustration of PPP measurements. The photon energies for pump and push pulses are 3.1 and 1.55 eV, respectively. (**B**) Pump-push–induced photoconductivity transient with the corresponding incident photon density of 0.1×10^{15} and 0.8×10^{15} cm^{-2}. The push pulse arrives ~8.2 ps after the pump pulse. (**C**) The push fluence–dependent double differential photoconductivity with a fixed incident pump photon density of 0.1×10^{15} cm^{-2}. The gray line shows the push-only photoconductivity transient without pump but with a push photon density of 1.6×10^{15} cm^{-2}.

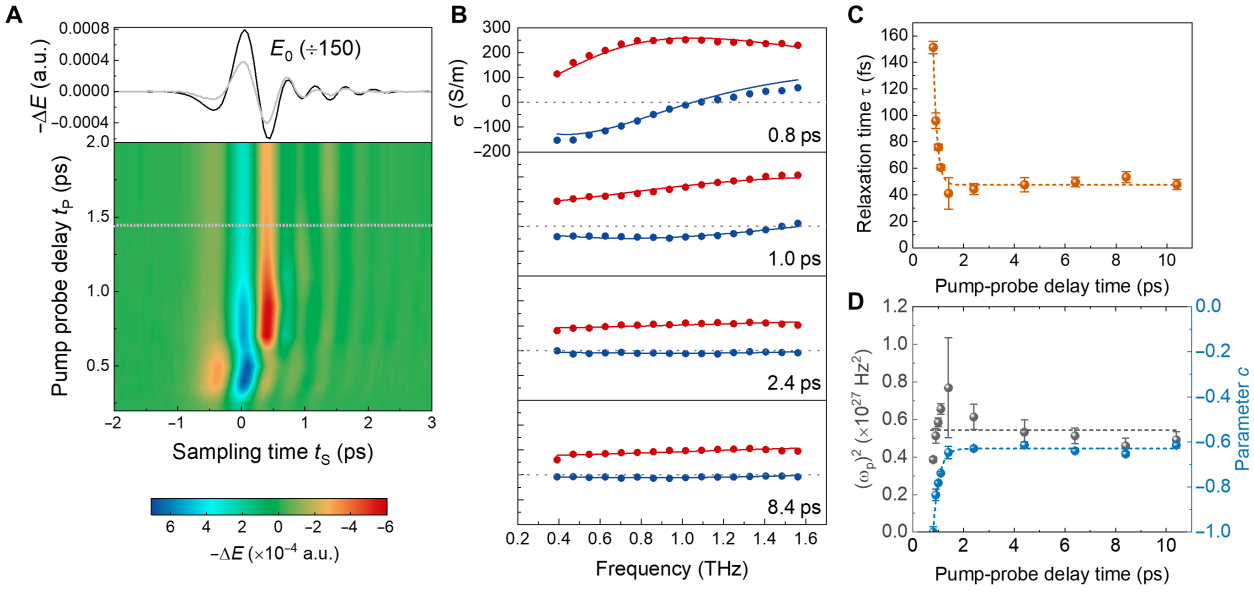

Fig. 4. Frequency-resolved terahertz photoconductivity spectra. (**A**) Pseudo-color representation of the two time-resolved terahertz electric field change $-\Delta E$, with a pump excitation wavelength of 400 nm and an absorbed photon density of ~1.02×10^{14} cm^{-2}. All data are measured at a fixed pump sampling delay time by moving the pump and sampling stages simultaneously (see the Supplementary Materials for more details). The gray line in the top panel shows an example of $-\Delta E$ at a fixed t_P, corresponding to the gray dotted line in the bottom panel. The black line is the transmitted terahertz electric field through the unexcited sample. (**B**) The complex frequency-resolved photoconductivity measured at various pump-probe delay times t_P (at 0.8, 1.0, 2.4, and 8.4 ps, respectively). The red and blue dots represent the real and imaginary components, respectively, of the measured complex photoconductivity; the corresponding solid lines represent the DS description as discussed in the main text. (**C** and **D**) The inferred charge relaxation time τ and square of the plasma frequency and parameter c, respectively, from the DS model as a function of t_P. The dashed lines serve as a guide to the eye.

One potential limitation of our TDS measurement protocol is that the sample conductivity should not be strongly dispersed, to ensure that the response can be approximated by a delta function in the time domain (*42*). For highly dispersive photoconductivity, the terahertz pulse passing through the photoexcited samples may become distorted, i.e., different frequency components will be delayed in time relative to one another. For this reason, we constrain our data analysis from 0.8 ps onward, where the dispersion in the photoconductivity is limited. In the Supplementary Materials, we further justify our choice of the time range for data analysis with extended discussions. The frequency-resolved photoconductivity can be well parameterized by a modified Drude model, the so-called Drude-Smith (DS) model, which reads (*26*, *43*)

$$\sigma(\omega) = \frac{\omega_p^2 \varepsilon_0 \tau}{1 - i\omega\tau}\left(1 + \frac{c}{1 - i\omega\tau}\right) \quad (1)$$

where ω_p is the plasma frequency ($\omega_p = \sqrt{\frac{n}{\varepsilon_0 \cdot m^*}}e$, m^* is the effective mass), τ is the DS relaxation time, ε_0 is the vacuum permittivity, and ω is the angular frequency. Different from the classical Drude model, the DS model introduces a parameter c (ranging from −1 to 0) to account for the anisotropic backscattering effect originating from, e.g., the presence of the grain boundary or interface. For $c = 0$, the DS model simplifies to the Drude model, which describes the free-carrier transport with isotropic momentum scattering. For $c = -1$, on the other hand, free charges are subject to 100% backscattering events. This model has been successfully applied to describe the charge carrier transport in a wide range of nanostructured semiconductors, including semiconducting polymers (*44*, *45*).

As demonstrated in Fig. 4B, the photoconductivity dispersion evolves between 1 and 3 ps. The DS parameterization allows quantifying this trend by displaying the parameter c and the DS relaxation time τ in Fig. 4 (C and D). The dispersion of the conductivity changes strongly from $c \approx -1$ and $\tau \approx 150$ fs for hot carriers at 0.8 ps following the excitation to $c \approx -0.63$ and $\tau \approx 50$ fs for cold carriers (established after ~2 ps). Note that the DS relaxation time τ is different from the momentum scattering time τ_D following the Drude model (*43*). On the other hand, τ and τ_D are positively correlated (*43*), so that τ reflects the trend of the time evolution of the charge momentum scattering time. As shown in Fig. 4C, the higher mobility of hot carriers is primarily due to the overall longer scattering time of the charged species. Furthermore, as illustrated in Fig. 4D, we observe that the value of parameter c is close to −1 for initial hot carriers exhibiting a long charge scattering time. This observation can be understood as follows: Hot carriers can traverse, between scattering events, a relatively long distance comparable to or exceeding the grain size or film thickness (both around 200 nm). Hence, the probability for preferential backscattering of hot carriers is larger than that of cold ones, explaining the variation in the parameter c. This also indicates that the hot carrier transport length can be larger than 200 nm. The inferred plasma frequency ω_p is constant within experimental uncertainty, indicating that there seems no substantial time-dependent variation in effective mass. Describing the conductivity with a fixed ω_p yields no change in the general trend for τ (see fig. S7). The ratio of charge relaxation times between hot and cold carriers coincides with the ~3-fold higher mobility of hot carriers than cold ones, as shown in Fig. 2C for a pump wavelength of 400 nm, i.e., a photon energy of 3.1 eV. Therefore, both the amplitude and dispersion of

the hot carrier conductivity indicate a higher mobility of hot carriers compared to cold ones in this double perovskite due to a reduced scattering rate experienced by hot carriers. Assuming $\tau_D \approx \tau = 150$ fs and $m^* = 0.35\ m_0$ (*21*), we estimate a remarkably high transient hot carrier mobility of 750 $cm^2\ V^{-1}\ s^{-1}$.

DISCUSSION

The observation of highly mobile hot carriers with reduced scattering rates in double perovskites can be accounted for by (quasi-)ballistic transport of thermalized hot carriers with sufficiently high kinetic energies. Hot carrier thermalization in Pb-based organic-inorganic perovskites has been reported to occur in an ultrafast, sub–150 fs time scale due to efficient carrier-carrier scattering (*3*). In principle, the thermalization process in perovskites is governed by efficient carrier-carrier scattering, and its scattering rate is expected to scale with $1/\varepsilon^2$ (with ε as the optical dielectric constant). As ε for both conventional Pb-based organic-inorganic perovskites and $Cs_2AgBiBr_6$ falls into a similar range (~5 to 7) (*3*, *23*), no substantial difference in thermalization time for both systems is expected. Therefore, one might expect a photoconductivity peak following the thermalization process - (100-200 fs) after optical excitations. In our terahertz studies, we probe the averaged photoconductivity, scattering, and thus mobility of charge carrier ensembles (including both electron and hole contribution) during the cooling process. For electrons, we expect the same photoconductivity rise as observed for other classes of perovskites (*15*, *33*). The slightly delayed "apparent" photoconductivity peak at 400 fs may be rationalized by taking into account the time-dependent photoconductivity contributions from both hot electrons and holes. The high conductivity of the early charge species following excitation and internal carrier thermalization originates from a highly energetic hot carrier population with sufficiently high kinetic energy, which can undergo (quasi-) ballistic transport (*13*, *14*). With increasing pump photon energy, for a given absorbed photon density, as shown in Fig. 2B, the fraction of hot carriers above an excess energy "threshold" for (quasi-) ballistic transport increases, leading to an increase in the transient hot carrier conductivity. Such a photoconductivity enhancement gradually reaches saturation (as shown in Fig. 2C), which may be attributed to the saturation in the electron temperature by increasing the pump photon energies (see section S10). During the cooling process (within 2 to 3 ps), the density of highly energetic hot carriers for ballistic transport decreases, and the photoconductivity drops correspondingly from the peak toward the cold carrier conductivity. Our discussion is also in line with the work of Gou *et al.* (*14*) on excess energy-dependent long-range hot carrier transport in $MAPbI_3$ studied by TA microscopy within the first few picoseconds. By directly measuring the terahertz photoconductivity, we are further able to provide mechanistic insights into the process. It is reduced charge scattering rather than reduced effective mass that gives rise to the high mobility. Moreover, we identify the dominant contribution of hot holes to the enhanced mobility. In principle, both electrons and holes with sufficiently high excess energy can undergo ballistic transport. The dominant role of hot holes in governing the hot carrier mobility in $Cs_2AgBiBr_6$ may lie in a peculiar feature in the band structure. The narrow energy range in the first conduction band of double perovskites limits the energetics of hot electrons following light absorption. Hence, for photoexcitation, in particular with photons with energies beyond direct band excitation (at ~2.8 eV), the excess energies of hot carriers distribute asymmetrically with much more energy into holes, leading to favorable (quasi-)ballistic transport conditions for hot holes.

To conclude, we observe an excess energy-dependent hot carrier mobility in $Cs_2AgBiBr_6$ double perovskite using terahertz spectroscopy. Upon excitation by photons with an excess energy beyond ~0.5 eV, hot carriers exhibit higher mobility than cold carriers. Using PPP spectroscopy and frequency-resolved photoconductivity measurements, we provide experimental evidence that such a mobility enhancement originates primarily from hot holes, which experience reduced momentum scattering compared to their cold states. We rationalize our observation by (quasi-)ballistic transport of thermalized hot holes above an energetic threshold in $Cs_2AgBiBr_6$. Our findings render $Cs_2AgBiBr_6$ double perovskite as a fascinating platform for studying the fundamentals of hot carrier transport and its exploitation toward efficient hot carrier–based optoelectronic devices.

MATERIALS AND METHODS

Sample preparation and characterization

$Cs_2AgBiBr_6$ single crystals were grown via controlled cooling. A mixture of 1.0 mmol of $BiBr_3$ (≥98%; Sigma-Aldrich) and 2.0 mmol of CsBr (99.9%; Sigma-Aldrich) in 10 ml of HBr (≥99.99%, 48 weight %; Honeywell Fluka) in a 40-ml vial was sonicated for 5 min. After adding 1.0 mmol of AgBr (≥99%; Chem-Lab), the suspension was sonicated for 5 min and then heated to 120°C to obtain a supersaturated solution. The mixture was cooled according to the following protocol: First, it was kept at 120°C for 3 hours, then cooled by 2°C $hour^{-1}$ to 100°C, and further by lower cooling rate of 1°C $hour^{-1}$ to 50°C. After that, milimeter-sized single crystals could be collected from the mixture by filtration. The crystals were washed with isopropanol [high-performance liquid chromatography (HPLC) grade; Sigma-Aldrich] and then dried in a vacuum oven at 60°C. The synthesis was performed under ambient atmospheric conditions. For the optical measurements, a 0.5 M solution of the crystals in dimethylsulfoxide was spin-coated on top of fused silica substrates (1 cm by 1 cm) resulting in uniform films with a thickness of ~200 nm. The samples are characterized by UV-vis spectroscopy, XRD, and atomic force microscopy.

OPTP and PPP spectroscopy

The OPTP and PPP spectrometer is driven by a commercial, regenerative amplified, mode-locked Ti:sapphire femtosecond laser with a 1-kHz repetition rate. The pulse duration is around 100 fs, and the central wavelength is ~800 nm. A single-cycle terahertz pulse is generated by optical rectification on a 1-mm-thick ZnTe crystal. The terahertz electrical field in the time domain is probed with an additional 800-nm sampling pulse via electro-optic effect on a second ZnTe crystal by varying the time delay between terahertz and sampling beam with an optical delay stage. The pump-probe delay is controlled by a second optical delay stage. In addition, a third delay stage is added controlling the pump-push delay time in the PPP measurement. For the optical excitation of 400 nm, it is produced by second harmonic generation from 800-nm light by beta barium borate crystal, while the other wavelengths are obtained by commercial optical parametric amplifier from Light Conversion.

SUPPLEMENTARY MATERIALS

Supplementary material for this article is available at https://science.org/doi/10.1126/sciadv.abj9066

REFERENCES AND NOTES

1. J. L. Oudar, D. Hulin, A. Migus, A. Antonetti, F. Alexandre, Subpicosecond spectral hole burning due to nonthermalized photoexcited carriers in GaAs. *Phys. Rev. Lett.* **55**, 2074–2077 (1985).
2. S. Hunsche, H. Heesel, A. Ewertz, H. Kurz, J. H. Collet, Spectral-hole burning and carrier thermalization in GaAs at room temperature. *Phys. Rev. B Condens. Matter* **48**, 17818–17826 (1993).
3. J. M. Richter, F. Branchi, F. V. de Almeida Camargo, B. Zhao, R. H. Friend, G. Cerullo, F. Deschler, Ultrafast carrier thermalization in lead iodide perovskite probed with two-dimensional electronic spectroscopy. *Nat. Commun.* **8**, 379 (2017).
4. M. Bernardi, D. Vigil-Fowler, J. Lischner, J. B. Neaton, S. G. Louie, Ab initio study of hot carriers in the first picosecond after sunlight absorption in silicon. *Phys. Rev. Lett.* **112**, 257402 (2014).
5. Y. Yang, D. P. Ostrowski, R. M. France, K. Zhu, J. van de Lagemaat, J. M. Luther, M. C. Beard, Observation of a hot-phonon bottleneck in lead-iodide perovskites. *Nat. Photonics* **10**, 53–59 (2016).
6. W. Shockley, H. J. Queisser, Detailed balance limit of efficiency of p-n junction solar cells. *J. Appl. Phys.* **32**, 510–519 (1961).
7. R. T. Ross, A. J. Nozik, Efficiency of hot-carrier solar energy converters. *J. Appl. Phys.* **53**, 3813–3818 (1982).
8. D.-T. Nguyen, L. Lombez, F. Gibelli, S. Boyer-Richard, A. Le Corre, O. Durand, J.-F. Guillemoles, Quantitative experimental assessment of hot carrier-enhanced solar cells at room temperature. *Nat. Energy* **3**, 236–242 (2018).
9. H. Esmaielpour, K. R. Dorman, D. K. Ferry, T. D. Mishima, M. B. Santos, V. R. Whiteside, I. R. Sellers, Exploiting intervalley scattering to harness hot carriers in III–V solar cells. *Nat. Energy* **5**, 336–343 (2020).
10. M. Bernardi, D. Vigil-Fowler, C. S. Ong, J. B. Neaton, S. G. Louie, Ab initio study of hot electrons in GaAs. *Proc. Natl. Acad. Sci. U.S.A.* **112**, 5291–5296 (2015).
11. D. Turchinovich, F. D'Angelo, M. Bonn, Femtosecond-timescale buildup of electron mobility in gaas observed via ultrabroadband transient terahertz spectroscopy. *Appl. Phys. Lett.* **110**, 121102 (2017).
12. H. Zhu, K. Miyata, Y. Fu, J. Wang, P. P. Joshi, D. Niesner, K. W. Williams, S. Jin, X.-Y. Zhu, Screening in crystalline liquids protects energetic carriers in hybrid perovskites. *Science* **353**, 1409–1413 (2016).
13. J. Sung, C. Schnedermann, L. Ni, A. Sadhanala, R. Y. S. Chen, C. Cho, L. Priest, J. M. Lim, H.-K. Kim, B. Monserrat, P. Kukura, A. Rao, Long-range ballistic propagation of carriers in methylammonium lead iodide perovskite thin films. *Nat. Phys.* **16**, 171–176 (2019).
14. Z. Gou, Y. Wan, M. Yang, J. Snaider, K. Zhu, L. Huang, Long-range hot-carrier transport in hybrid perovskites visualized by ultrafast microscopy. *Science* **356**, 59–62 (2017).
15. M. Monti, K. D. G. I. Jayawardena, E. Butler-Caddle, R. M. I. Bandara, J. M. Woolley, M. Staniforth, S. R. P. Silva, J. Lloyd-Hughes, Hot carriers in mixed Pb-Sn halide perovskite semiconductors cool slowly while retaining their electrical mobility. *Phys. Rev. B* **102**, 245204 (2020).
16. R. L. Z. Hoye, L. Eyre, F. Wei, F. Brivio, A. Sadhanala, S. Sun, W. Li, K. H. L. Zhang, J. L. MacManus-Driscoll, P. D. Bristowe, R. H. Friend, A. K. Cheetham, F. Deschler, Fundamental carrier lifetime exceeding 1 μs in $Cs_2AgBiBr_6$ double perovskite. *Adv. Mater. Interfaces* **5**, 1800464 (2018).
17. J. A. Steele, W. Pan, C. Martin, M. Keshavarz, E. Debroye, H. Yuan, S. Banerjee, E. Fron, D. Jonckheere, C. W. Kim, W. Baekelant, G. Niu, J. Tang, J. Vanacken, M. Van der Auweraer, J. Hofkens, M. B. J. Roeffaers, Photophysical pathways in highly sensitive $Cs_2AgBiBr_6$ double-perovskite single-crystal x-ray detectors. *Adv. Mater.* **30**, e1804450 (2018).
18. W. Ning, F. Wang, B. Wu, J. Lu, Z. Yan, X. Liu, Y. Tao, J. M. Liu, W. Huang, M. Fahlman, L. Hultman, T. C. Sum, F. Gao, Long electron-hole diffusion length in high-quality lead-free double perovskite films. *Adv. Mater.* **30**, e1706246 (2018).
19. M. Delor, A. H. Slavney, N. R. Wolf, M. R. Filip, J. B. Neaton, H. I. Karunadasa, N. S. Ginsberg, Carrier diffusion lengths exceeding 1 μm despite trap-limited transport in halide double perovskites. *ACS Energy Lett.* **5**, 1337–1345 (2020).
20. W. Pan, H. Wu, J. Luo, Z. Deng, C. Ge, C. Chen, X. Jiang, W.-J. Yin, G. Niu, L. Zhu, L. Yin, Y. Zhou, Q. Xie, X. Ke, M. Sui, J. Tang, $Cs_2AgBiBr_6$ single-crystal x-ray detectors with a low detection limit. *Nat. Photonics* **11**, 726–732 (2017).
21. M. Keshavarz, E. Debroye, M. Ottesen, C. Martin, H. Zhang, E. Fron, R. Küchler, J. A. Steele, M. Bremholm, J. Van de Vondel, H. I. Wang, M. Bonn, M. B. J. Roeffaers, S. Wiedmann, J. Hofkens, Tuning the structural and optoelectronic properties of $Cs_2AgBiBr_6$ double-perovskite single crystals through alkali-metal substitution. *Adv. Mater.* **32**, 2001878 (2020).
22. L. Schade, A. D. Wright, R. D. Johnson, M. Dollmann, B. Wenger, P. K. Nayak, D. Prabhakaran, L. M. Herz, R. Nicholas, H. J. Snaith, P. G. Radaelli, Structural and optical properties of $Cs_2AgBiBr_6$ double perovskite. *ACS Energy Lett.* **4**, 299–305 (2018).
23. B. Wu, W. Ning, Q. Xu, M. Manjappa, M. Feng, S. Ye, J. Fu, S. Lie, T. Yin, F. Wang, Strong self-trapping by deformation potential limits photovoltaic performance in bismuth double perovskite. *Sci. Adv.* **7**, eabd3160 (2021).
24. A. D. Wright, L. R. V. Buizza, K. J. Savill, G. Longo, H. J. Snaith, M. B. Johnston, L. M. Herz, Ultrafast excited-state localization in $Cs_2AgBiBr_6$ double perovskite. *J. Phys. Chem. Lett.* **12**, 3352–3360 (2021).
25. H. Nemec, F. Kadlec, S. Surendran, P. Kuzel, P. Jungwirth, Ultrafast far-infrared dynamics probed by terahertz pulses: A frequency domain approach. I. Model systems. *J. Chem. Phys.* **122**, 104503 (2005).
26. R. Ulbricht, E. Hendry, J. Shan, T. F. Heinz, M. Bonn, Carrier dynamics in semiconductors studied with time-resolved terahertz spectroscopy. *Rev. Mod. Phys.* **83**, 543–586 (2011).
27. A. Schmitz, L. L. Schaberg, S. Sirotinskaya, M. Pantaler, D. C. Lupascu, N. Benson, G. Bacher, Fine structure of the optical absorption resonance in $Cs_2AgBiBr_6$ double perovskite thin films. *ACS Energy Lett.* **5**, 559–565 (2020).
28. Z. Xiao, W. Meng, J. Wang, Y. Yan, Thermodynamic stability and defect chemistry of bismuth-based lead-free double perovskites. *ChemSusChem* **9**, 2628–2633 (2016).
29. J. A. Steele, P. Puech, M. Keshavarz, R. Yang, S. Banerjee, E. Debroye, C. W. Kim, H. Yuan, N. H. Heo, J. Vanacken, A. Walsh, J. Hofkens, M. B. J. Roeffaers, Giant electron-phonon coupling and deep conduction band resonance in metal halide double perovskite. *ACS Nano* **12**, 8081–8090 (2018).
30. G. Longo, S. Mahesh, L. R. V. Buizza, A. D. Wright, A. J. Ramadan, M. Abdi-Jalebi, P. K. Nayak, L. M. Herz, H. J. Snaith, Understanding the performance-limiting factors of $Cs_2AgBiBr_6$ double-perovskite solar cells. *ACS Energy Lett.* **5**, 2200–2207 (2020).
31. M. C. Beard, G. M. Turner, C. A. Schmuttenmaer, Transient photoconductivity in GaAs as measured by time-resolved terahertz spectroscopy. *Phys. Rev. B* **62**, 15764–15777 (2000).
32. P. Uhd Jepsen, W. Schairer, I. H. Libon, U. Lemmer, N. E. Hecker, M. Birkholz, K. Lips, M. Schall, Ultrafast carrier trapping in microcrystalline silicon observed in optical pump–terahertz probe measurements. *Appl. Phys. Lett.* **79**, 1291–1293 (2001).
33. S. A. Bretschneider, I. Ivanov, H. I. Wang, K. Miyata, X. Zhu, M. Bonn, Quantifying polaron formation and charge carrier cooling in lead-iodide perovskites. *Adv. Mater.* **30**, e1707312 (2018).
34. H. Zhang, E. Debroye, J. A. Steele, M. B. J. Roeffaers, J. Hofkens, H. I. Wang, M. Bonn, Highly mobile large polarons in black phase $CsPbI_3$. *ACS Energy Lett.* **6**, 568–573 (2021).
35. X. Y. Zhu, V. Podzorov, Charge carriers in hybrid organic-inorganic lead halide perovskites might be protected as large polarons. *J. Phys. Chem. Lett.* **6**, 4758–4761 (2015).
36. S. F. Maehrlein, P. P. Joshi, L. Huber, F. Wang, M. Cherasse, Y. Liu, D. M. Juraschek, E. Mosconi, D. Meggiolaro, F. De Angelis, X. Y. Zhu, Decoding ultrafast polarization responses in lead halide perovskites by the two-dimensional optical kerr effect. *Proc. Natl. Acad. Sci. U.S.A.* **118**, e2022268118 (2021).
37. A. A. Bakulin, A. Rao, V. G. Pavelyev, P. H. van Loosdrecht, M. S. Pshenichnikov, D. Niedzialek, J. Cornil, D. Beljonne, R. H. Friend, The role of driving energy and delocalized states for charge separation in organic semiconductors. *Science* **335**, 1340–1344 (2012).
38. E. T. McClure, M. R. Ball, W. Windl, P. M. Woodward, Cs_2AgBiX_6 (X = Br, Cl): New visible light absorbing, lead-free halide perovskite semiconductors. *Chem. Mater.* **28**, 1348–1354 (2016).
39. K. Z. Du, W. Meng, X. Wang, Y. Yan, D. B. Mitzi, Bandgap engineering of lead-free double perovskite $Cs_2AgBiBr_6$ through trivalent metal alloying. *Angew. Chem. Int. Ed. Eng.* **56**, 8158–8162 (2017).
40. M. Palummo, E. Berrios, D. Varsano, G. Giorgi, Optical properties of lead-free double perovskites by ab initio excited-state methods. *ACS Energy Lett.* **5**, 457–463 (2020).
41. H.-K. Nienhuys, V. Sundström, Intrinsic complications in the analysis of optical-pump, terahertz probe experiments. *Phys. Rev. B* **71**, 235110 (2005).
42. E. Hendry, M. Koeberg, F. Wang, H. Zhang, C. de Mello Donega, D. Vanmaekelbergh, M. Bonn, Direct observation of electron-to-hole energy transfer in CdSe quantum dots. *Phys. Rev. Lett.* **96**, 057408 (2006).
43. T. L. Cocker, D. Baillie, M. Buruma, L. V. Titova, R. D. Sydora, F. Marsiglio, F. A. Hegmann, Microscopic origin of the Drude-Smith model. *Phys. Rev. B* **96**, 205439 (2017).
44. I. Ivanov, Y. Hu, S. Osella, U. Beser, H. I. Wang, D. Beljonne, A. Narita, K. Mullen, D. Turchinovich, M. Bonn, Role of edge engineering in photoconductivity of graphene nanoribbons. *J. Am. Chem. Soc.* **139**, 7982–7988 (2017).
45. S. A. Jensen, R. Ulbricht, A. Narita, X. Feng, K. Mullen, T. Hertel, D. Turchinovich, M. Bonn, Ultrafast photoconductivity of graphene nanoribbons and carbon nanotubes. *Nano Lett.* **13**, 5925–5930 (2013).
46. J. M. Schins, E. Hendry, M. Bonn, H. G. Muller, Retrieving the susceptibility from time-resolved terahertz experiments. *J. Chem. Phys.* **127**, 094308 (2007).
47. E. Hendry, *Charge Dynamics in Novel Semiconductors* (University of Amsterdam, 2005).

Acknowledgments: We thank Y. Yan and X. Wang at the University of Toledo and our colleagues K. Krewer, A. Tries, X. Jia, and M. Ballabio for discussions. **Funding:** S.F. acknowledges fellowship support from Chinese Scholarship Council (CSC). E.D. acknowledges

financial support from the Research Foundation Flanders (FWO) (FWO grant nos. 12O3719N and S002019N) and from KU Leuven (KUL grant no. STG/21/010). L.D.V. acknowledges support from EU Horizon 2020 Framework Programme (grant no. 811284). **Author contributions:** H.I.W. and M.B. designed the project. H.Z. conducted terahertz measurements. E.D. synthesized the $Cs_2AgBiBr_6$ perovskites. All authors discussed and analyzed the results. H.Z. and H.I.W drafted the paper with input from all authors. All authors have given approval to the final version of the manuscript. **Competing interests:** The authors declare that they have no competing interests. **Data and materials availability:** All data needed to evaluate the conclusions in the paper are present in the paper and/or the Supplementary Materials.

Submitted 10 June 2021
Accepted 4 November 2021
Published 22 December 2021
10.1126/sciadv.abj9066

ScienceAdvances

Highly mobile hot holes in CsAgBiBr double perovskite

Heng ZhangElke DebroyeWenhao ZhengShuai FuLucia D. VirgilioPushpendra KumarMischa BonnHai I. Wang

Sci. Adv., 7 (52), eabj9066. • DOI: 10.1126/sciadv.abj9066

Science Advances (ISSN) is published by the American Association for the Advancement of Science. 1200 New York Avenue NW, Washington, DC 20005. The title *Science Advances* is a registered trademark of AAAS.